ARTICLES
https://doi.org/10.1038/s41563-019-0292-9
nature materials

Bioinspired neuron-like electronics

Xiao Yang[1,4], Tao Zhou[1,4], Theodore J. Zwang[1,4], Guosong Hong[1], Yunlong Zhao[1], Robert D. Viveros[2], Tian-Ming Fu[1], Teng Gao[1] and Charles M. Lieber[1,2,3*]

As an important application of functional biomaterials, neural probes have contributed substantially to studying the brain. Bioinspired and biomimetic strategies have begun to be applied to the development of neural probes, although these and previous generations of probes have had structural and mechanical dissimilarities from their neuron targets that lead to neuronal loss, neuroinflammatory responses and measurement instabilities. Here, we present a bioinspired design for neural probes—neuron-like electronics (NeuE)—where the key building blocks mimic the subcellular structural features and mechanical properties of neurons. Full three-dimensional mapping of implanted NeuE–brain interfaces highlights the structural indistinguishability and intimate interpenetration of NeuE and neurons. Time-dependent histology and electrophysiology studies further reveal a structurally and functionally stable interface with the neuronal and glial networks shortly following implantation, thus opening opportunities for next-generation brain–machine interfaces. Finally, the NeuE subcellular structural features are shown to facilitate migration of endogenous neural progenitor cells, thus holding promise as an electrically active platform for transplantation-free regenerative medicine.

The design of materials using concepts inspired by and/or mimicking biology is an attractive strategy for the development of innovative materials and has led to exciting advances across a variety of fields, including controlling crystallization kinetics[1], developing mechanically tough materials[2] and engineering the design and functionality of biomaterials[3,4]. Biomaterials have also been used in the development of multifunctional neural probes that will help to understand the brain[5,6]. Recently, the design of implanted neural probes has begun to benefit from the advantages and opportunities afforded by bioinspired and biomimetic design strategies[7]. These strategies include designing a stimuli-responsive material with dynamic stiffness[8] for easy insertion of probes, and utilizing vein compression to reduce tissue trauma[9]. In view of these successes in implementing bioinspired concepts in neural interfacing, it is noteworthy that neural probes that adapt the structural or mechanical features of cells have not been explored.

Evidence suggests that structural and mechanical differences between neural probes and neuron targets in the brain can lead to disruption of the native tissue[10,11] that negatively impacts the capability to stably interrogate and modulate natural physiological activity over time[5,6,12–15]. Research aimed at reducing these disparities has focused on improving mechanical properties by optimizing the device geometry[12,16–20] or using more flexible materials[21], including mesh probes that achieve tissue-like flexibility[16–18]. Nevertheless, in terms of structure and mechanics, existing probes remain essentially 'foreign' to the primary neuron building blocks of the brain, presenting a dichotomy with the successful concepts of bioinspired design.

Design and characteristics of neuron-like electronics

As a step towards biomimetic electronics that address the baseline distinctions between implanted probes and the fundamental neuron component of the brain, we have focused on a probe unit building block that is structurally and mechanically similar to a neuron at the subcellular level (Fig. 1a), although not yet with the functional complexity. In our biomimetic design the sizes of the metal recording electrode and interconnect, which constitute the probe building block, match those of the soma and neurite of a typical pyramidal neuron. Moreover, the interconnect and axon have similar flexibility (details are provided in the following) and the thin polymer insulation is analogous to the myelin sheath; both assist in the propagation of electrical signals from the electrode and soma, respectively. Finally, the neuron-like building blocks are organized to construct an open three-dimensional (3D) electronic network—neuron-like electronics (NeuE)—with structure and topology similar to neural networks (Fig. 1a, inset).

The NeuE was fabricated using photolithography[17], where the neurite-like interconnects consist of polymer/metal/polymer structures with polymer and metal widths of 4 and 2 μm or 1 and 0.6 μm, respectively, with a total thickness of ~0.9 μm for the two designs studied (Supplementary Table 1 and Methods). The soma-like platinum recording electrodes were supported on the lower polymer layer (Supplementary Fig. 1). Images of a pyramidal neuron and the two different building blocks used for the NeuE (Fig. 1b, Supplementary Fig. 2a,b and Methods) highlight the biomimetic structural characteristics, including the similarity in sizes of the smaller unit interconnect with dendritic branches. The fabrication of NeuE is detailed in the Methods and key probe layers are shown in Supplementary Fig. 1.

A key physical consequence of the neuron-like dimensions of the NeuE building blocks is that the mechanical stiffness is reduced 5–20 times compared to the most flexible state-of-the-art reported probes[17,19,20,22] due to the reduction in feature widths to match the diameter of neurites (Fig. 1c and Supplementary Note 1). The calculated bending stiffness of the NeuE neurite-like interconnect is comparable to the axon of a neuron (Fig. 1c and Supplementary Note 1)[23,24], thus matching the flexibility of a subcellular component for the first time. Also, the estimated percentage of occupied volume for the implanted NeuE probes, 0.07–0.3% (Supplementary Table 1 and Supplementary Note 2) for the designs in Fig. 1b, is distinct from conventional solid probes[5,6] that exclude all cells from their occupied volume, and is up to 20 times lower than recent macroporous

[1]Department of Chemistry and Chemical Biology, Harvard University, Cambridge, MA, USA. [2]John A. Paulson School of Engineering and Applied Sciences, Harvard University, Cambridge, MA, USA. [3]Center for Brain Science, Harvard University, Cambridge, MA, USA. [4]These authors contributed equally: Xiao Yang, Tao Zhou, Theodore J. Zwang. *e-mail: cml@cmliris.harvard.edu

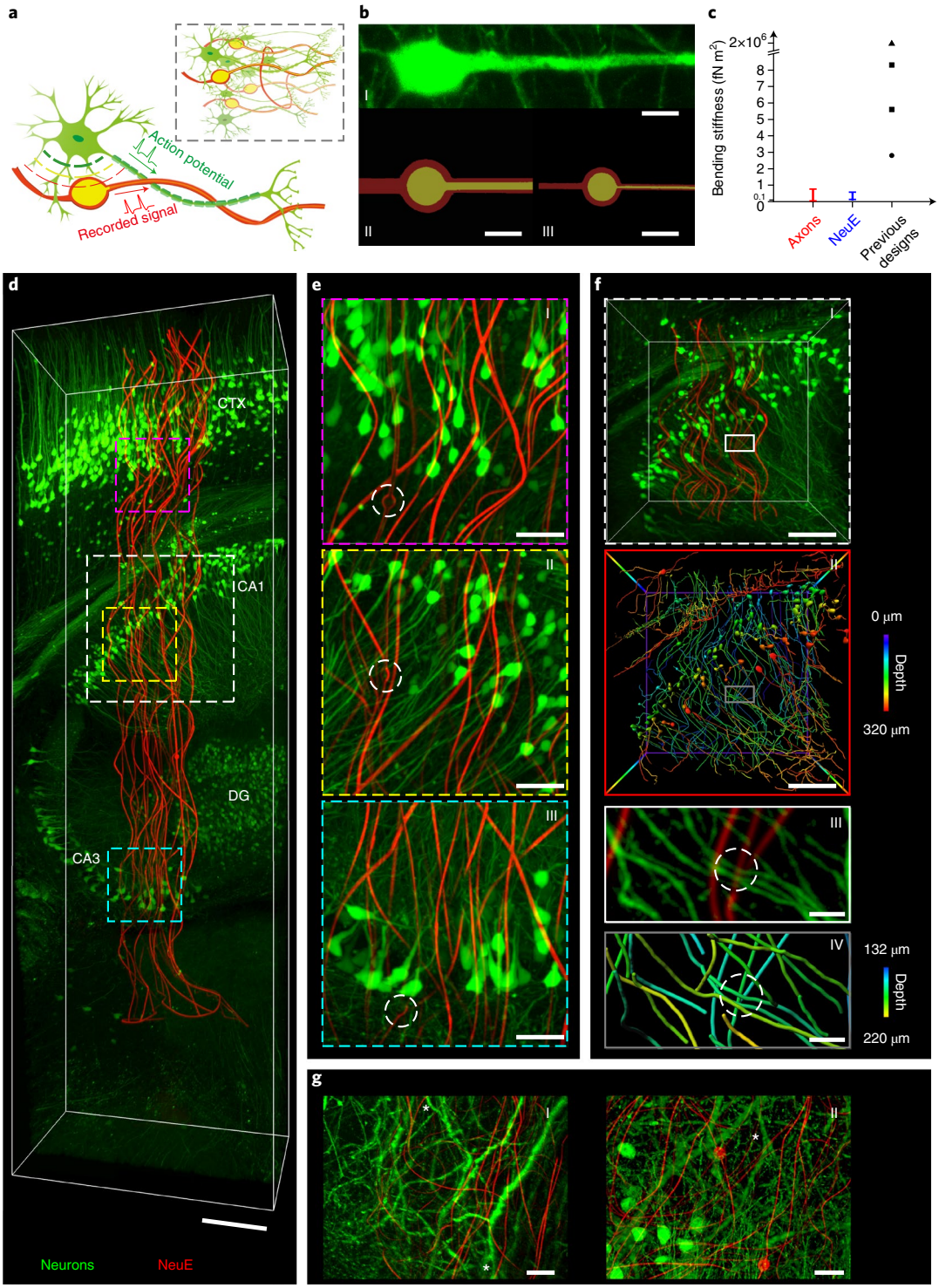

Fig. 1 | Design and characterization of NeuE, and 3D mapping of its neural interface. a, Schematics showing the structural similarity between NeuE and neurons from the subcellular level to the network level (inset). Neurons, green; electrodes and interconnects, yellow; polymer layers, red. **b**, Fluorescence microscope image of a neuron (I) and false-coloured scanning electron microscope (SEM) images of two NeuE designs (II and III). Raw SEM images are shown in Supplementary Fig. 2. Scale bars, 10 µm. **c**, Bending stiffness of axons, NeuE and examples of previously reported state-of-the-art mesh[17] (circle), fibre[19,20] (triangle) and thread[22] probes (squares). **d**, 3D reconstructed interface between neurons (green) and NeuE (red) at 6 weeks post-implantation. Scale bar, 200 µm. 3D mapping was repeated on $N=3$ independent samples. Additional fluorescence images and quantitative analyses are shown in Supplementary Figs. 6 and 7. **e**, High-resolution images of the volumes highlighted by magenta (I), yellow (II) and cyan (III) dashed boxes in **d**. Electrodes are indicated by white dashed circles. Scale bars, 50 µm. **f**, Close-up images of the white dashed box in **d**. I and II correspond to standard fluorescence and depth-coded images, respectively. III and IV are close-up views indicated by the white and grey boxes in I and II, respectively, highlighting the junction between neurites and the NeuE neurite-like interconnect (white dashed circles). Colour codes for depth are shown in the frame in II and the colour bars to the right. Scale bars, 100 µm (I and II), 20 µm (III and IV). **g**, Close-up 3D neural interface of the smaller NeuE (**b**, III) in additional independent samples near cornu ammonis 1 (CA1) (I) and dentate gyrus (DG) (II) at 2 weeks post-injection. White asterisks indicate dendritic branches. Scale bars, 20 µm.

mesh probes[17]. Here we focus on 16-channel NeuE probes, but note that higher channel numbers should be achievable without sacrificing the flexibility and porosity by using higher-resolution fabrication to integrate multiple metal interconnect lines within a given neurite-like element[25,26].

Similar structure and 3D interpenetration with neurons

We asked how these unique features of NeuE probes affect the interface with neurons within the brain by full 3D mapping of the probe and surrounding brain tissue with subcellular resolution (Supplementary Fig. 3 and Methods) at different times post-implantation. We covalently bound a rhodamine derivative within the bulk of the polymer layers of the NeuE probes to provide stable conjugation and fluorescence under physiological conditions (Supplementary Fig. 4 and Methods). Precise targeted delivery of NeuE probes into live mice was performed using a stereotaxic injection method as described previously (see Methods)[27]. The NeuE probes were implanted into the hippocampus (HIP) through the cortex (CTX) of transgenic mouse lines expressing either yellow fluorescent proteins (YFPs) in neurons (Thy1-YFP-H)[28] or green fluorescent proteins (GFPs) in astrocytes (GFAP-GFP)[29]. A representative 3D reconstructed image of the NeuE and neurons at 6 weeks post-injection (Fig. 1d and Supplementary Video 1) highlights the similar sizes of the neurite-like interconnects and neuron neurites, the flexibility of these biomimetic 'neurites' and interpenetration of the NeuE and neurons from CTX through the CA3 region of the HIP. These and other key features are even more evident in higher-resolution images of the CTX (Fig. 1e,I), CA1 (Fig. 1e,II) and CA3 (Fig. 1e,III), which show the structural similarity between recording electrodes and neuron soma, as well as the interpenetrating interconnects and neurites. The capability to spatially resolve electrodes (white dashed circles in Fig. 1e) relative to surrounding neurons in situ with micrometre resolution allows for correlating structural and functional mapping, as will be discussed later, and has not been possible previously for implanted multi-electrode neural probes.

The structural similarity and interpenetration of the NeuE probe with neurons were further examined by colour-encoding their positions as a function of depth within 3D images. Comparison of zoomed-in views of CA1 with standard fluorophore (Fig. 1f,I) and depth-coding (Fig. 1f,II and Supplementary Video 2) indicates that NeuE integrates in neural tissue without noticeable disturbance, and, indeed, it is difficult to distinguish the interwoven NeuE and neuron structures. Examination of neurite-like interconnects and neuron neurites (Fig. 1f,III,IV and Supplementary Video 3) highlights this latter point, which emphasizes the structural biomimetic nature of the NeuE, and strikingly shows that neuron neurites and NeuE neurite-like interconnects make close contact that might in future be developed into artificial neuro-electronics junctions or synapses. In addition, 3D images (Fig. 1g) of the smaller NeuE design (Fig. 1b,III) at 2 weeks post-implantation show similar integration, with the smaller neurite-like interconnects being comparable to dendritic branches (white asterisks), and show that the overall NeuE probes exhibit greater flexibility within the tissue, consistent with its smaller bending stiffness.

Time-dependent brain interface

We also asked how the implanted NeuE affects the distribution of key cell types across the HIP and CTX as a function of time post-implantation in Thy1-YFP-H and GFAP-GFP transgenic mice, which have been previously validated for assessing tissue integration and foreign body response on the basis of in vivo and in vitro imaging studies[22,28,29]. Histology imaging and quantitative analyses have been replicated on multiple ($N=3$) independent samples containing NeuE probes at 2 days, 2 weeks, 6 weeks and 3 months post-implantation for both transgenic mouse lines, and show similar results, as detailed in the following (Fig. 2 and Supplementary Figs. 5–7). Representative 3D images of NeuE/neuron (Fig. 2a and Supplementary Fig. 5a) and NeuE/astrocyte (Fig. 2b and Supplementary Fig. 5b) interfaces show a relatively uniform cell distribution without obvious depletion of neurons or enhancements of astrocytes near the NeuE from the earliest time of analysis onward.

We quantified the time-dependent post-implantation response by analysing the cell distributions in volumes containing NeuE and the dentate gyrus (DG), CA1 or the CTX (Fig. 2c and Supplementary Note 4). Representative tissue volumes (Supplementary Fig. 8a) encompass the NeuE probe and most of the cells in each of these three brain regions. Although some displacement of existing tissue occurs during insertion of the glass capillary, which is withdrawn from the brain tissue during injection of the NeuE, normalized neuron fluorescence intensity (Fig. 2c) demonstrated there is substantial neuronal density in the interior of the NeuE probe as early as 2 days. Moreover, the neurons exhibit a fully endogenous distribution in the DG, CA1 and CTX regions at times extending from 2 weeks. Analyses of astrocyte labelled samples (Fig. 2d) further show the astrocyte density is close to baseline at 2 and 14 days, and is uniform at endogenous levels at longer times. These results for neurons and astrocytes are quantitatively similar to control samples of the same brain regions in the absence of implantation (Supplementary Fig. 9 and Supplementary Note 4). We repeated the time-dependent histology studies for two distinct sets of Thy1-YFP-H and GFAP-GFP mice at 2 days and 2, 6 and 12 weeks (16 mice in total; Supplementary Table 2). Representative fluorescence images (Supplementary Fig. 6) and quantitative analyses (Supplementary Fig. 7) demonstrate the reproducibility of these results. Comparison of the normalized fluorescence intensity from tissue volumes (Supplementary Fig. 8a) versus thin horizontal slices (Supplementary Fig. 8b) relative to the NeuE probes for both neurons and astrocytes also show similar overall results, although there are substantially smaller fluctuations in the fluorescence intensities analysed on the 3D volume samples (Supplementary Fig. 8c,d).

In addition, the samples shown in Fig. 2b and Supplementary Fig. 5b were subject to tissue clearing[30,31] followed by microglia immunostaining (see Methods). Fluorescence images (Supplementary Fig. 5c) and quantitative fluorescence intensity analyses (Supplementary Fig. 5d) show a uniform distribution of microglia around NeuE probes through the CTX, CA1 and DG over this time period, consistent with the absence of an immune response inferred from analyses of neuron and astrocyte distributions. Additionally, sham injection control experiments and subsequent immunostaining (Supplementary Fig. 10 and Methods) show a minimal immune response, as revealed by the close to endogenous levels of astrocytes and microglia at the site of injection.

These data contrast the typical depletion of neurons and proliferation of astrocytes and microglia close to the external boundary of solid probes[10,11], as well as the decrease in neuron density within the interior and increase in astrocyte density at the surface boundary of conventional macroporous mesh probes even after 2 weeks post-implantation[18]. Hence, the full 3D analyses provide a quantifiable measure of the substantially lower invasiveness of the NeuE probes. We suggest that the bioinspired design, which mimics the size features and mechanical properties of neurons as well as occupying less than 0.3% volume once implanted (Supplementary Table 1), is crucial to achieving the observed results. Specifically, these features may allow for the migration of cells and the diffusion and dispersion of pro-inflammatory signalling proteins[32] that ultimately leads to this attractive behaviour of not activating astrocytes or microglia.

Stable single-unit recording following implantation

We asked whether it would be possible to follow the activity of the same neurons from the time of implantation onwards and, moreover, to correlate the measured activity with the subcellular resolution

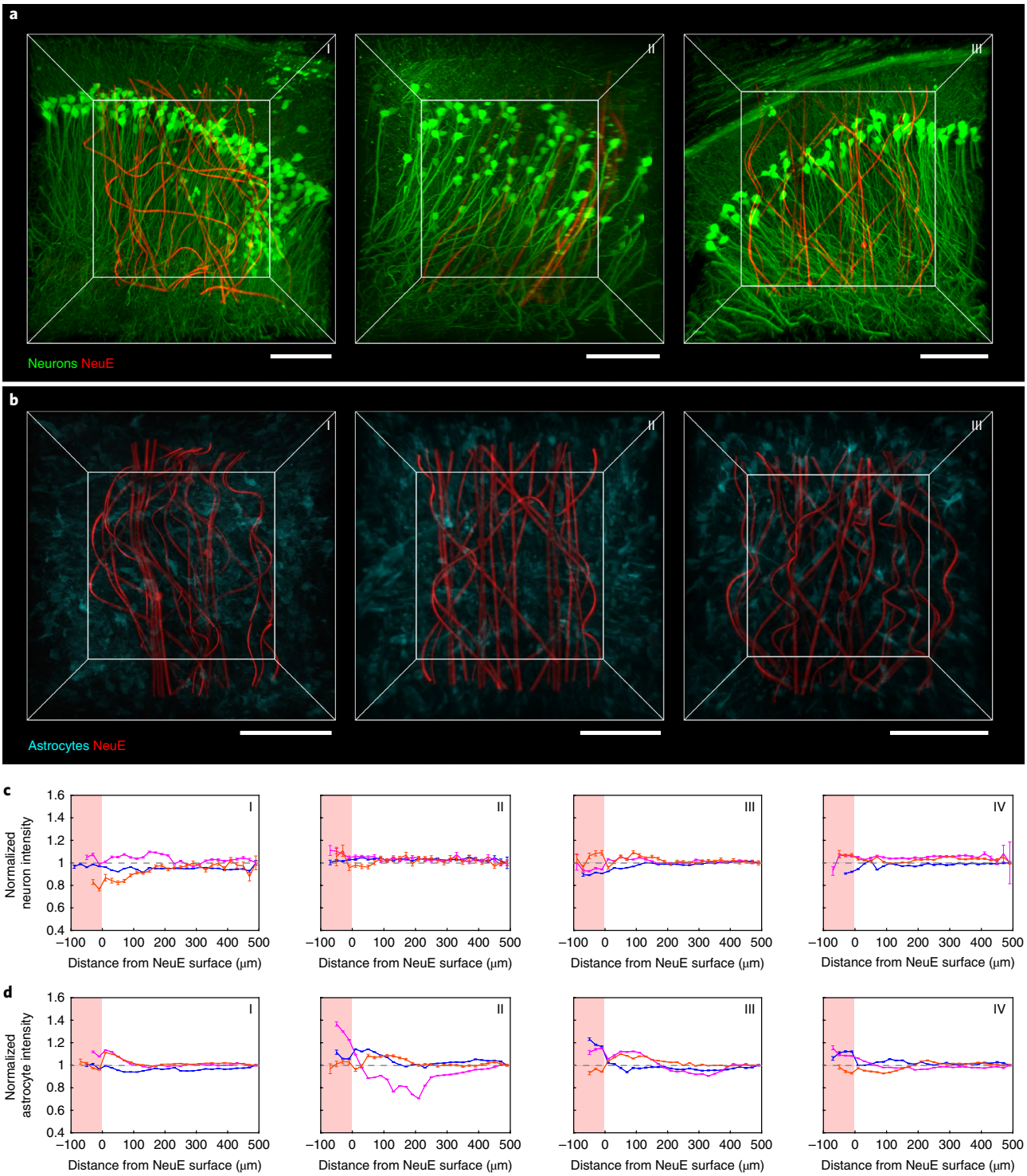

Fig. 2 | Time-dependent 3D histology studies of NeuE–brain interfaces. a, 3D interfaces between NeuE (red) and neurons (green) at 2 days (I), 2 weeks (II) and 3 months (III) post-implantation. Scale bars, 100 μm. **b**, 3D interfaces between NeuE (red) and astrocytes (cyan) at 2 days (I), 2 weeks (II) and 3 months (III) post-implantation. Scale bars, 100 μm. **c**,**d**, Normalized fluorescence intensity of neurons (**c**) and astrocytes (**d**) as a function of distance from the 3D NeuE boundary at CTX (orange), hippocampal CA1 (magenta) and DG (blue) at 2 days (I), 2 weeks (II), 6 weeks (III) and 3 months (IV) post-implantation. The pink-shaded regions indicate tissue volumes within the interior of the NeuE. The relative signal was obtained by normalizing the fluorescence intensity with the baseline value defined as the fluorescence intensity averaged over a range of 480–500 μm away (grey dashed horizontal lines; Supplementary Note 4). The tissue volumes for analysis depend on the specific structures of the distinct brain regions, as shown in Supplementary Fig. 5a,b. All error bars reflect ±1 s.e.m. There is substantial neuronal density, 91 ± 12% (mean ± s.d.) of baseline, in the interior of the NeuE probe boundary as early as 2 days, and this increases to 100 ± 7% of baseline at times extending from 2 weeks when the neurons exhibit a fully endogenous distribution in the DG, CA1 and CTX regions. The astrocyte density is 107 ± 8% of baseline at 2 and 14 days, and is uniform at the endogenous level, 102 ± 3%, at longer times. Time-dependent 3D histology studies have been repeated on $N = 3$ independent samples; additional fluorescence images and quantitative analyses are shown in Supplementary Figs. 6 and 7.

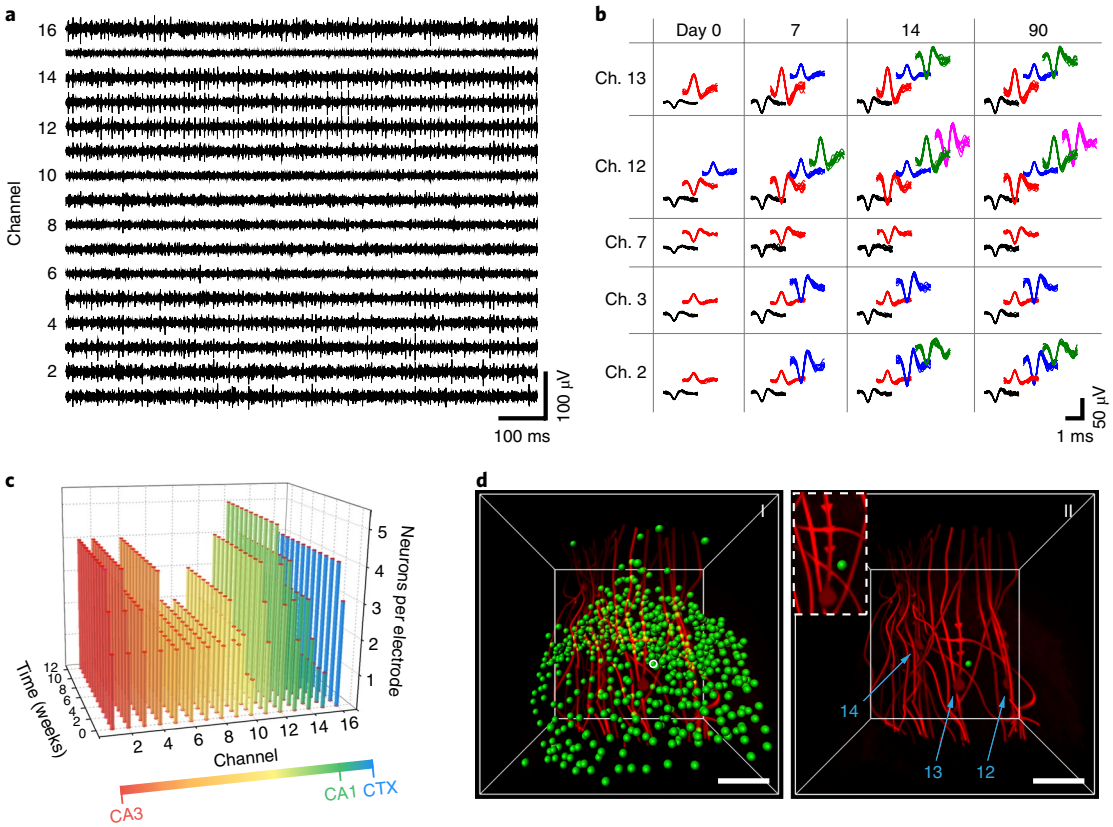

Fig. 3 | Functional interrogation with NeuE. a, Representative 16-channel single-unit spike traces at 7 days post-injection. The *x* and *y* axes represent recording time and voltage. **b**, Time evolution of spikes of principal component analysis clustered single units from five representative channels over 3 months post-injection. For each channel, each distinct colour in the sorted spikes represents a unique identified neuron. **c**, 3D bar chart of the number of distinct neurons recorded per electrode as a function of the time post-injection. Bar colours are coded according to the brain regions, as shown in the colour bar at the bottom. Larger numbers of isolated neuron signals were recorded in channels located in CA3 and CA1 regions of the HIP, and lower numbers in channels located in the lower-density space between CA3 and CA1. Time-dependent electrophysiology studies were repeated on $N=3$ independent animals. Data and analyses from additional replicates are shown in Supplementary Figs. 18 and 19. **d**, 3D images of NeuE near the CA1 subfield. Green dots in I indicate the soma of imaged neurons after segmentation. The neuron triangulated by electrodes 12, 13 and 14 is highlighted by a white circle. II shows the relative positioning of the triangulated neuron (green dot) with respect to electrodes 12, 13 and 14 (highlighted by light blue arrows). Inset, Magnified view of the triangulated neuron. Scale bars, 50 μm. 3D mapping and channel indexing of all the electrodes ($N=16$) are shown in Supplementary Fig. 11.

topology of the imaged NeuE and neurons in 3D. NeuE probes were implanted with 16 addressable electrodes distributed across the HIP and CTX, and the probe–brain was imaged at the 3 month recording endpoint to spatially resolve the barcoded electrodes with respect to the surrounding neurons (Supplementary Fig. 11 and Methods). Multiplexed recordings (Fig. 3a and Supplementary Fig. 12) exhibit stable single-unit spikes across the HIP through the CTX regions from the time of initial implantation (day 0) through to the endpoint of the measurements (day 90), where the position of the NeuE probe was fixed following initial implantation. This contrasts with the position adjustments often used to reacquire active neuron signals between recording sessions for conventional probes[33,34]. Overall analyses of the single-unit spike signal-to-noise ratios (SNRs; Supplementary Fig. 13) show nearly constant values from the time of implantation onward. In addition, the electrode interfacial impedances exhibited relatively constant values over time, and the interchannel impedances show minimal crosstalk between channels (Supplementary Fig. 14 and Methods).

Given this global single-unit recording stability, we asked whether it was possible to illuminate the single neuron activity as a function of time by tracking isolated neurons (Supplementary Note 5). A comparison of sorted spikes from each channel for days 0, 7, 14 and 90 (Fig. 3b and Supplementary Fig. 15) highlights several points. First, the isolated neurons, which are highlighted by different colour spike waveforms in each of the 16 channels, are remarkably constant over the 3 months of recording. There is no evidence of loss of isolated neuron signals over this period, although new neuron signals are observed in 11 out of 16 channels during the first 2 weeks (Fig. 3b,c and Supplementary Fig. 15). These results contrast with the decrease in recorded neurons with time for conventional neural probes[34,35], as well as the ~1 month period necessary to first see stabilized and well-isolated single units with mesh electronics[17]. Second, the number of recorded neurons varies across channels in a way that correlates with the neuron soma density in different HIP subfields.

Third, we have carried out analyses to assess the strength of our above conclusion based on sorted neuron spikes. Principal component analysis[35,36] shows the same clusters with relatively constant positions in the first and second principal component plane (PC1–PC2) over the 12 weeks studied (Supplementary Fig. 16), thus demonstrating single-unit stability over time. In addition, L-ratio analysis (Supplementary Note 5)[37,38] shows values of <0.05 for all detected neurons (Supplementary Table 3) and indicates minimal contamination between isolated units and thus good unit separation.

Furthermore, quantitative waveform autocorrelation analysis for the same neuron recorded on different days (Supplementary Fig. 17 and Supplementary Note 5)[34] demonstrates that the neuron spikes have consistent characteristic waveform features over time, which is indicative of chronic recording stability.

Finally, we repeated the time-dependent electrophysiology studies and analyses for two additional mice implanted with NeuE probes (Supplementary Figs. 18 and 19). These results are consistent with the data presented in Fig. 3 (and Supplementary Figs. 12–17), with a total of 40 initially connected channels, demonstrating the reproducibility of the stable single neuron recording and tracking of NeuE probes. Furthermore, analyses of mechanical stress in deformed NeuE elements characterized in 3D images of the implanted probes demonstrate that the maximum stress is well below the fatigue failure limit of the SU-8 material[39] used in fabrication (Supplementary Note 6), thus indicating that NeuE probes could exhibit long-term mechanical robustness beyond the 3 months studied.

The combined electrophysiology and imaging data allowed us to ask whether the intact interface between the NeuE electrodes and neurons across the HIP and CTX could allow the spatial coordinates of the same spiking neuron detected by three nearby recording electrodes to be determined by triangulation (Supplementary Note 5)[40,41]. Triangulation has been used previously[40,41], although it has not been possible to register the electrode–neuron positions at the cellular scale as probes must be extracted for histology studies[33,34,40]. An example is that of electrodes 12, 13 and 14, which record the same neuron (Fig. 3d); this was identified (Fig. 3d,II) from the population of CA1 neurons surrounding these electrodes (Fig. 3d,I) by in situ reconstruction of the 3D electrodes–neurons interface. We suggest this capability of mapping recorded cells onto the undisturbed imaged brain structures could open new opportunities to link directly functional and topological circuits within their physiological context. This is distinct from reported methods combining in vivo imaging and subsequent in vitro brain slice electrophysiology, where additional neuron transduction for structural marker expression[42] or fluorescent microspheres[43] are required to re-identify the same neurons. Moreover, this registration-free in situ 3D mapping capability opens the possibility of directly correlating experience-dependent neuronal activity with the underlying neuronal connectivity when combined with recent neuronal activity markers such as immediate early genes[44].

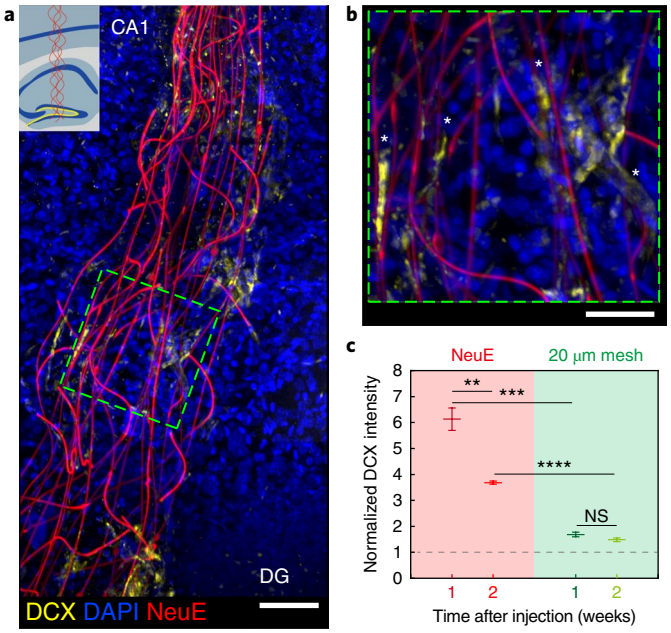

Fig. 4 | NeuE facilitates migration of NPC-derived newborn neurons. **a**, A representative 3D image showing the distribution of DCX$^+$ newborn neurons along NeuE at 1 week post-implantation. Yellow, blue and red colours represent DCX, DAPI and NeuE, respectively. Scale bar, 100 μm. Inset, Schematic showing the injection site, with dark blue, yellow and red colours indicating principal cell body layers, SGZ and NeuE, respectively. **b**, Magnified view of the green dashed box in **a**, demonstrating that some DCX$^+$ cells show neurite spreading associated and aligned with the neurite-like NeuE structure (highlighted by white asterisks). Scale bar, 50 μm. **c**, Normalized DCX intensity at 0–20 μm near the NeuE or 20 μm mesh normalized against baseline values remote to the probe (grey dashed horizontal line; Supplementary Note 4). Each condition was repeated on three independent tissue volumes. Additional data are shown in Supplementary Figs. 20 and 21. All error bars reflect ±1 s.e.m. Top to bottom, $P=5\times10^{-3}$ ($^{**}P<1\times10^{-2}$), $P=6\times10^{-4}$ ($^{***}P<1\times10^{-3}$), $P=2\times10^{-5}$ ($^{****}P<1\times10^{-4}$), $P=1.4\times10^{-1}$ (NS, not significant, $P>5\times10^{-2}$); two-tailed *t*-test.

NeuE promotes the migration of newborn neurons

The 3D interpenetration of neurons through NeuE probes and the observation of new spiking neuron signals at early times led us to ask whether native neural progenitor cells (NPCs) originating from the subgranular zone (SGZ) of the HIP[45,46] migrate and concurrently develop into newborn neurons along the neurite-like structure of the NeuE since probes are implanted with ends touching or spanning the SGZ (Fig. 4a inset and Supplementary Fig. 20a). The presence of NPC-derived newborn neurons was assessed by staining NeuE-implanted tissue samples with doublecortin (DCX) antibody for newborn neurons[45,46] and 4′,6-diamidino-2-phenylindole (DAPI) for nuclear DNA, following tissue clearing (see Methods)[30,31]. Representative 3D images of brain tissue at 1 week post-implantation (Fig. 4a,b) show substantial DCX$^+$ cells associated and aligned with the NeuE structure, yet little or no DCX staining of DAPI$^+$ cells further away from the probe.

To gain further insight into the importance of the NeuE biomimetic structure in promoting the association and migration of DCX$^+$ newborn neurons, we also assessed NeuE-injected samples collected at 2 weeks post-implantation (Supplementary Fig. 20) and controls using the significantly larger (20 μm width features) mesh electronics (Supplementary Fig. 21). Overall, there is a statistically significant decrease ($P<0.01$) in the enhancement of DCX$^+$ cells near NeuE at 2 weeks versus 1 week (Fig. 4c, Supplementary Fig. 20 and Supplementary Note 4) and, strikingly, the 20 μm control mesh shows a substantial approximately threefold decrease ($P<0.001$) in DCX$^+$ cells compared to NeuE at both time points (Fig. 4c, Supplementary Fig. 21 and Supplementary Note 4). These quantitative data suggest that the biomimetic neurite-like topographical features of NeuE may modulate the endogenous NPC-derived cell behaviour including adhesion and migration[47], and help to explain the rapid tissue healing and the emergence of 'new' spiking neurons.

Summary and outlook

The NeuE represents a strong case for the use of bioinspiration and biomimicry as tools for the design of innovative materials and devices for neurotechnology. In contrast to other state-of-the-art electrophysiology probes[12–15,17–20,22,34,35], NeuE probes match the subcellular feature sizes and mechanical properties of neurons. NeuE probes elicit negligible immune response compared to other probes[12,14,17–20] and exhibit seamless interpenetrating interfaces with the brain from day 2 post-implantation onwards. In addition, NeuE probes demonstrate stable single-unit recording of individual cells in the nearly native physiological context without loss in recording quality from shortly after implantation to at least 3 months. We suggest that these characteristics arise from matching the structural and mechanical properties to the local cellular components within

the microenvironment, which largely eliminates micromotion and tissue damage associated with signal instability[48]. In addition, NeuE is a substrate for the migration of newborn neurons, suggesting its potential to direct cells towards sites of damage where they could help repair or regenerate damaged tissues, and as a multimodal platform for actively remodelling tissue while simultaneously monitoring such changes. Nevertheless, multifunctional integration that allows for simultaneous optical, electrical and chemical interrogation[19,20] and high spatial integration that allows for simultaneous recording of a larger number of neurons[26] represent interesting directions to pursue in the future, for example, by integrating higher-resolution fabrication methods. In addition, given that the current NeuE design has virtually eliminated structural and mechanical distinctions with the fundamental neuron component of the brain, we suggest that this can serve as an ideal starting point to exploit biochemical modification strategies[12,13] to endow it with added functionality. More generally, we believe that the neural interface of bioinspired NeuE, which is structurally and mechanically indistinguishable from neurons, gliosis-free, functionally stable and pro-regenerative, can open opportunities for next-generation brain–machine interfaces and biomedical therapeutics.

Online content

Any methods, additional references, Nature Research reporting summaries, source data, statements of data availability and associated accession codes are available at https://doi.org/10.1038/s41563-019-0292-9.

Received: 17 August 2018; Accepted: 16 January 2019;
Published online: 25 February 2019

References

1. Ma, X. et al. Tuning crystallization pathways through sequence engineering of biomimetic polymers. *Nat. Mater.* **16**, 767–774 (2017).
2. Fratzl, P., Kolednik, O., Fischer, F. D. & Dean, M. N. The mechanics of tessellations—bioinspired strategies for fracture resistance. *Chem. Soc. Rev.* **45**, 252–267 (2016).
3. Green, J. J. & Elisseeff, J. H. Mimicking biological functionality with polymers for biomedical applications. *Nature* **540**, 386–394 (2016).
4. Sadtler, K. et al. Design, clinical translation and immunological response of biomaterials in regenerative medicine. *Nat. Rev. Mater.* **1**, 16040 (2016).
5. Chen, R., Canales, A. & Anikeeva, P. Neural recording and modulation technologies. *Nat. Rev. Mater.* **2**, 16093 (2017).
6. Feiner, R. & Dvir, T. Tissue–electronics interfaces: from implantable devices to engineered tissues. *Nat. Rev. Mater.* **3**, 17076 (2017).
7. Shoffstall, A. J. & Capadona, J. R. Bioinspired materials and systems for neural interfacing. *Curr. Opin. Biomed. Eng.* **6**, 110–119 (2018).
8. Capadona, J. R., Shanmuganathan, K., Tyler, D. J., Rowan, S. J. & Weder, C. Stimuli-responsive polymer nanocomposites inspired by the sea cucumber dermis. *Science* **319**, 1370–1374 (2008).
9. Smith, D. W. et al. Internal jugular vein compression mitigates traumatic axonal injury in a rat model by reducing the intracranial slosh effect. *Neurosurgery* **70**, 740–746 (2012).
10. Polikov, V. S., Tresco, P. A. & Reichert, W. M. Response of brain tissue to chronically implanted neural electrodes. *J. Neurosci. Methods* **148**, 1–18 (2005).
11. Salatino, J. W., Ludwig, K. A., Kozai, T. D. Y. & Purcell, E. K. Glial responses to implanted electrodes in the brain. *Nat. Biomed. Eng.* **1**, 862–877 (2017).
12. Kozai, T. D. Y. et al. Ultrasmall implantable composite microelectrodes with bioactive surfaces for chronic neural interfaces. *Nat. Mater.* **11**, 1065–1073 (2012).
13. Charkhkar, H. et al. Chronic intracortical neural recordings using microelectrode arrays coated with PEDOT–TFB. *Acta Biomater.* **32**, 57–67 (2016).
14. Bedell, H. W. et al. Targeting CD14 on blood derived cells improves intracortical microelectrode performance. *Biomaterials* **163**, 163–173 (2018).
15. Arati, S., Subramaniam, D. R. & Jit, M. Long-term changes in the material properties of brain tissue at the implant–tissue interface. *J. Neural Eng.* **10**, 066001 (2013).
16. Liu, J. et al. Syringe-injectable electronics. *Nat. Nanotechnol.* **10**, 629–636 (2015).
17. Fu, T.-M. et al. Stable long-term chronic brain mapping at the single-neuron level. *Nat. Methods* **13**, 875–882 (2016).
18. Zhou, T. et al. Syringe-injectable mesh electronics integrate seamlessly with minimal chronic immune response in the brain. *Proc. Natl Acad. Sci. USA* **114**, 5894–5899 (2017).
19. Canales, A. et al. Multifunctional fibers for simultaneous optical, electrical and chemical interrogation of neural circuits in vivo. *Nat. Biotechnol.* **33**, 277–284 (2015).
20. Park, S. et al. One-step optogenetics with multifunctional flexible polymer fibers. *Nat. Neurosci.* **20**, 612–619 (2017).
21. Minev, I. R. et al. Electronic dura mater for long-term multimodal neural interfaces. *Science* **347**, 159–163 (2015).
22. Luan, L. et al. Ultraflexible nanoelectronic probes form reliable, glial scar–free neural integration.*Sci. Adv.* **3**, e1601966 (2017).
23. Garcia, J., Pena, J., McHugh, S. & Jerusalem, A. A model of the spatially dependent mechanical properties of the axon during its growth. *Comput. Model. Eng. Sci.* **87**, 411–432 (2012).
24. Wang, S. S.-H. et al. Functional trade-offs in white matter axonal scaling. *J. Neurosci.* **28**, 4047–4056 (2008).
25. Fu, T.-M., Hong, G., Viveros, R. D., Zhou, T. & Lieber, C. M. Highly scalable multichannel mesh electronics for stable chronic brain electrophysiology. *Proc. Natl Acad. Sci. USA* **114**, E10046–E10055 (2017).
26. Jun, J. J. et al. Fully integrated silicon probes for high-density recording of neural activity. *Nature* **551**, 232–236 (2017).
27. Hong, G. S. et al. Syringe injectable electronics: precise targeted delivery with quantitative input/output connectivity. *Nano Lett.* **15**, 6979–6984 (2015).
28. Feng, G. et al. Imaging neuronal subsets in transgenic mice expressing multiple spectral variants of GFP. *Neuron* **28**, 41–51 (2000).
29. Zhuo, L. et al. Live astrocytes visualized by green fluorescent protein in transgenic mice. *Dev. Biol.* **187**, 36–42 (1997).
30. Chung, K. et al. Structural and molecular interrogation of intact biological systems. *Nature* **497**, 332–337 (2013).
31. Yang, B. et al. Single-cell phenotyping within transparent intact tissue through whole-body clearing. *Cell* **158**, 945–958 (2014).
32. Saxena, T. & Bellamkonda, R. V. A sensor web for neurons. *Nat. Mater.* **14**, 1190–1191 (2015).
33. Igarashi, K. M., Lu, L., Colgin, L. L., Moser, M.-B. & Moser, E. I. Coordination of entorhinal–hippocampal ensemble activity during associative learning. *Nature* **510**, 143–147 (2014).
34. Jackson, A. & Fetz, E. E. Compact movable microwire array for long-term chronic unit recording in cerebral cortex of primates. *J. Neurophysiol.* **98**, 3109–3118 (2007).
35. Dickey, A. S., Suminski, A., Amit, Y. & Hatsopoulos, N. G. Single-unit stability using chronically implanted multielectrode arrays. *J. Neurophysiol.* **102**, 1331–1339 (2009).
36. Quiroga, R. Q., Nadasdy, Z. & Ben-Shaul, Y. Unsupervised spike detection and sorting with wavelets and superparamagnetic clustering. *Neural Comput.* **16**, 1661–1687 (2004).
37. Schmitzer-Torbert, N., Jackson, J., Henze, D., Harris, K. & Redish, A. D. Quantitative measures of cluster quality for use in extracellular recordings. *Neuroscience* **131**, 1–11 (2005).
38. Schmitzer-Torbert, N. & Redish, A. D. Neuronal activity in the rodent dorsal striatum in sequential navigation: separation of spatial and reward responses on the multiple T task. *J. Neurophysiol.* **91**, 2259–2272 (2004).
39. Spratley, J. P. F., Ward, M. C. L. & Hall, P. S. Bending characteristics of SU-8. *IET Micro Nano Lett.* **2**, 20–23 (2007).
40. Jog, M. S. et al. Tetrode technology: advances in implantable hardware, neuroimaging, and data analysis techniques. *J. Neurosci. Methods* **117**, 141–152 (2002).
41. Buzsáki, G. et al. Tools for probing local circuits: high-density silicon probes combined with optogenetics. *Neuron* **86**, 92–105 (2015).
42. Weiler, S. et al. High-yield in vitro recordings from neurons functionally characterized in vivo. *Nat. Protoc.* **13**, 1275–1293 (2018).
43. Cossell, L. et al. Functional organization of excitatory synaptic strength in primary visual cortex. *Nature* **518**, 399–403 (2015).
44. Liu, X. et al. Optogenetic stimulation of a hippocampal engram activates fear memory recall. *Nature* **484**, 381–385 (2012).
45. Gonçalves, J. T., Schafer, S. T. & Gage, F. H. Adult neurogenesis in the hippocampus: from stem cells to behavior. *Cell* **167**, 897–914 (2016).
46. Ming, G.-l & Song, H. Adult neurogenesis in the mammalian central nervous system. *Annu. Rev. Neurosci.* **28**, 223–250 (2005).
47. Reza, M. et al. In vivo migration of endogenous brain progenitor cells guided by an injectable peptide amphiphile biomaterial. *J. Tissue Eng. Regen. Med.* **12**, e2123–e2133 (2018).
48. James, C. B. et al. Failure mode analysis of silicon-based intracortical microelectrode arrays in non-human primates. *J. Neural Eng.* **10**, 066014 (2013).

Acknowledgements

The authors thank D. Richardson and S. Terclavers for help with image acquisition, data handling and critical discussion, and J. Huang for assistance with recording instrumentation. This work is supported by the National Institute on Drug Abuse of

the National Institutes of Health (1R21DA043985-01), a NIH Director's Pioneer Award (1DP1EB025835-01) and the Air Force Office of Scientific Research (FA9550-14-1-0136) (to C.M.L.), the Simmons Awards (to X.Y.) and an American Heart Association Postdoctoral Fellowship (16POST27250219) and NIH Pathway to Independence Award (1K99AG056636-02) (to G.H.). This work was performed in part at the Harvard Center for Biological Imaging (HCBI) and Harvard University Center for Nanoscale Systems (CNS), a member of the National Nanotechnology Coordinated Infrastructure Network (NNCI) supported by the National Science Foundation.

Author contributions

X.Y. and C.M.L. designed the experiments. X.Y., T.Z., T.J.Z., G.H., Y.Z., R.D.V., T.-M.F. and T.G. performed the experiments. X.Y., T.Z., T.J.Z. and C.M.L. analysed the data. X.Y. and C.M.L. wrote the paper. All authors discussed the results, revised or commented on the manuscript.

Competing interests

The authors declare no competing interests.

Additional information

Supplementary information is available for this paper at https://doi.org/10.1038/s41563-019-0292-9.

Reprints and permissions information is available at www.nature.com/reprints.

Correspondence and requests for materials should be addressed to C.M.L.

Publisher's note: Springer Nature remains neutral with regard to jurisdictional claims in published maps and institutional affiliations.

Methods

Design and fabrication of NeuE. The design and structural parameters of NeuE are distinct from previous reports[16–18], although the overall fabrication approach is similar to our previous reports[16–18]. The parameters of the two NeuE designs used for these studies are summarized in Supplementary Table 1. Barcodes based on a unique combination of triangles and circles associated with electrodes (Supplementary Fig. 11b) were also introduced for indexing the recording electrodes in electrophysiological experiments. Here we focus on 16-channel NeuE probes, but note that higher channel numbers can be achieved[25] without varying the reported designs by using higher-resolution fabrication[26].

The key fabrication steps for NeuE probes are as follows. (1) A 100-nm-thick Ni sacrificial layer was thermally evaporated (Sharon Vacuum Co.) onto a 3-inch Si wafer (n-type 0.005 Ω cm, 600 nm thermal oxide, NOVA Electronic Materials), which was pre-cleaned with oxygen plasma (100 W, 5 min; AST Products). (2) Negative photoresist SU-8 (SU-8 2000.5; MicroChem) was mixed with Lissamine rhodamine B ethylenediamine (RhBen; ~10 μg ml^{-1}; Thermo Fisher Scientific) and placed in the dark at room temperature (RT) for 3 days. The primary amine groups of RhBen covalently react with the epoxide groups of SU-8 to afford stable fluorescence labelling[49]. To eliminate any possible undissolved RhBen, the SU-8/RhBen solution was then centrifuged (Thermo Fisher Scientific) at 10,000 r.p.m. for 3 min immediately before use. The supernatant of SU-8/RhBen solution was spin-coated on the Si wafer to a thickness of ~420 nm, pre-baked sequentially at 65 °C for 1 min and 95 °C for 4 min, and then patterned by photolithography with a mask aligner (SUSS MA6 mask aligner, SUSS MicroTec). After photolithography exposure, the Si wafer was post-baked sequentially at 65 °C for 3 min and 95 °C for 3 min. (3) The SU-8 photoresist was developed (SU-8 Developer, MicroChem) for 2 min, rinsed with isopropanol, dried with N_2 and hard baked at 180 °C for 1 h. (4) The Si wafer was then treated with oxygen plasma (50 W, 30 s), spin-coated with MCC Primer 80/20 and LOR 3A resist (MicroChem) and baked at 180 °C for 5 min. For NeuE design-1, Shipley 1805 positive photoresist (Microposit, Dow Chemical Company) was spin-coated on the Si wafer and baked at 115 °C for 5 min. The positive resist was patterned by photolithography (SUSS MA6 mask aligner) and developed (MF-CD-26, Microposit, Dow Chemical Company) for 90 s. For smaller NeuE design-2, diluted S1805 (1:3 (vol:vol) diluted in Thinner-P, Microchem) was spin-coated on the Si wafer and baked at 115 °C for 1 min. The positive resist was patterned by photolithography with a maskless aligner (MLA150) and developed (MF-CD-26) for 30 s. (5) After a flood exposure of the whole wafer, a 3-nm-thick Cr layer and a 100-nm-thick Au layer were sequentially deposited by electron-beam evaporation (Denton Vacuum), followed by a liftoff step (MF-CD-26) for the Au interconnect lines. (6) Steps 4 and 5 were repeated for photolithography patterning and deposition of Pt recording electrodes (3-nm-thick Cr and 50-nm-thick Pt). (7) Steps 2 and 3 were repeated for photolithography patterning of the top SU-8 layer as the encapsulation and insulating layer of the metal interconnect lines. After hard baking the top SU-8 layer at 180 °C for 1 h, the Si wafer was hard baked again at 190–195 °C for 1 h to allow interdiffusion of the bottom and top SU-8 layers to yield an effectively monolithic component. (8) To release NeuE probes, the Si wafer was cleaned with oxygen plasma (50 W, 30 s) and then transferred to a Ni etchant solution comprising 40% $FeCl_3$:39% HCl:H_2O = 1:1:20 for 60–90 min. Released NeuE probes were rinsed with deionized (DI) water, soaked in an aqueous solution of poly-D-lysine (1.0 mg ml^{-1}, M_w = 70,000–150,000, Sigma-Aldrich) for 24 h and then transferred to 1 × PBS solution (HyClone, GE Healthcare Life Sciences). Immediately before implantation, NeuE probes were sterilized as described in the following.

Structure characterization of NeuE. Zeiss Ultra Plus Field Emission SEM was used to characterize the structure of the NeuE building block components. The typical accelerating voltage was 0.6 kV. False colours were used for the presentation of Fig. 1b based on the raw images shown in Supplementary Fig. 2a,b, where SU-8 was rendered red and metal was rendered yellow.

Impedance characterization of NeuE. The electrical impedance of each recording electrode at 1 kHz was measured by the Intan system (Supplementary Fig. 14a), as detailed in the section Chronic electrophysiological recording from awake and restrained mice.

To characterize the frequency-dependent interchannel leakage impedance, impedance was measured on adjacent SU-8 passivated Au interconnects while immersed in 1 × PBS to approximate the in vivo recording environment, using an Agilent B1500A semiconductor device parameter analyser (Agilent Technologies) with a B1520AFG multifrequency capacitance measurement unit (Agilent Technologies). Measurements were taken from 1 kHz to 10 kHz (most relevant to single-unit spike recording).

Vertebrate animal subjects. Adult (6–8 weeks, 25–35 g) male B6.Cg-Tg(Thy1-YFP)HJrs/J (Thy1-YFP-H, stock no. 003782, The Jackson Laboratory), B6.Cg-Tg(Thy1-YFP)16Jrs/J (Thy1-YFP-16, stock no. 003709, The Jackson Laboratory), FVB/N-Tg(GFAPGFP)14Mes/J (GFAP-GFP, stock no. 003257, The Jackson Laboratory) and C57BL/6J mice (stock no. 000664, The Jackson Laboratory) were used in the study. Exclusion criteria were pre-established: animals with substantial acute implantation damage (>50 μl of initial liquid injection volume) or damage of a major blood vessel were discarded from further experiments.

All procedures were approved by the Animal Care and Use Committee of Harvard University. The animal care and use programmes at Harvard University meet the requirements of federal law (89–544 and 91–579) and NIH regulations and are also accredited by the American Association for Accreditation of Laboratory Animal Care (AAALAC). Before surgical procedures, animals were group-housed on a 12 h:12 h light:dark schedule in the Harvard University Biology Research Infrastructure (BRI) and fed with food and water ad libitum as appropriate. Animals were housed individually after surgical procedures.

In vivo mouse survival surgery. *Stereotaxic injection of NeuE in mouse brains.* In vivo injection of NeuE probes into live mice was performed using a controlled stereotaxic injection method as described previously[17,27] and reproduced here for completeness. All metal tools in direct contact with the animal subjects were bead-sterilized (Fine Science Tools) for 1 h before use, and all plastic tools in direct contact with the animal subjects were sterilized with 70% ethanol and rinsed with sterile DI water and sterile 1 × PBS before use. The NeuE probes were sterilized with 70% ethanol followed by rinsing in sterile DI water and sterile 1 × PBS before injection, and then loaded into sterile glass capillaries with an inner diameter of 400 μm and outer diameter of 550 μm (Produstrial). Mice were anaesthetized by intraperitoneal injection of a mixture of 75 mg kg^{-1} (body weight) of ketamine (Patterson Veterinary Supply) and 1 mg kg^{-1} dexdomitor (Orion). The degree of anaesthesia was verified via toe pinch before surgery started. A homeothermic blanket (Harvard Apparatus) was set to 37 °C and placed underneath the anaesthetized mouse. The anaesthetized mouse was placed in a stereotaxic frame (Lab Standard Stereotaxic Instrument, Stoelting Co.) equipped with two ear bars and one nose clamp. Puralube vet ointment (Dechra Pharmaceuticals) was applied on both eyes to moisturize the eye surface throughout the operation. Hair removal lotion (Nair, Church & Dwight) was applied to the scalp for depilation and Betadine surgical scrub (Purdue Products) was applied to sterilize the depilated scalp skin. A sterile scalpel was used to make a 5 mm longitudinal incision in the scalp along the sagittal sinus. The scalp skin was resected to expose a 5 mm × 5 mm portion of the skull.

In the surgeries for electrophysiological recording, Metabond adhesive luting cement (Parkell) was applied over the exposed cranial bone to prepare the skull surface for mounting the electronics later. A 1 mm burr hole was drilled using a dental drill (Micromotor with On/Off Pedal 110/220, Grobet USA) with the following stereotaxic coordinates: anteroposterior, −4.96 mm; mediolateral, 3.10 mm. The dura was carefully incised and resected using a sterile 27-gauge needle (PrecisionGlide, Becton Dickinson), then a sterilized 0–80 set screw (18-8 stainless steel cup point set screw, outer diameter 1.52 mm, groove diameter 1.14 mm, length 4.76 mm; McMaster-Carr Supply Company) was screwed into this 1 mm burr hole to a depth of 500 μm to serve as the grounding and reference electrode. Metabond adhesive luting cement was used to fix the junction between the screw and the skull.

A 1-mm-diameter burr hole was drilled for the injection of NeuE according to the following stereotaxic coordinates: anteroposterior, −2.30 mm; mediolateral, 1.75 mm; dorsoventral, 2.00 mm. The dura was removed from the burr hole, and sterile 1 × PBS was swabbed on the skull surface to keep it moist throughout the surgery. NeuE was injected into the targeted brain region using the controlled injection method reported previously[27]. In brief, the glass needle loaded with sterilized NeuE was inserted in the micropipette holder, which was connected to a 5 ml syringe (Becton Dickinson), which was pre-filled with 1 × PBS and mounted on a syringe pump (PHD 2000, Harvard Apparatus). The micropipette holder was mounted on a stereotaxic stage equipped with a motorized linear translation stage (860A motorizer and 460A linear stage, Newport) that could move the stereotaxic arm in the *z* direction with a constant preset velocity ranging from 0.05 to 0.5 mm s^{-1}. The needle was positioned at the surface of exposed brain tissue and then inserted into the brain tissue to the desired coordinates, which, when coupled with a rational design of electrode distribution, allows for the placement of electrodes at particular locations within the brain. Controllable injection was carried out by synchronizing the syringe pump with the motorized linear translation stage, with a typical liquid injection rate of 5–15 ml h^{-1} and a typical translational stage retraction velocity of 0.2–0.5 mm s^{-1}. The volumetric flow rate and needle retraction velocity were adjusted such that the upper part of NeuE, which was visualized through an eyepiece camera (DCC1240C, Thorlabs), remained stationary in the field of view. The total injection volume was usually 5–50 μl over the 2 mm length of injection. Control experiments with sham injections were performed in a similar manner without NeuE implantation, but with the injection of about 30 μl of 1 × PBS. Additional details of the implantation process are available at http://meshelectronics.org/protocols.html#injection.

Suture closure for 3D mapping surgeries. After implantation of the NeuE, the scalp was closed with 3M Vetbond tissue adhesive. Triple antibiotic ointment (WATER-JEL Technologies) was applied copiously on the closure.

Electrical connection of NeuE for chronic recordings. After injection of the NeuE into the targeted region of the mouse brain, the glass capillary was repositioned over

a flexible flat cable (FFC, Premo-Flex, Molex), and then the remaining part of the NeuE was expelled from the capillary and unfolded onto the FFC to expose the input–output connection pads. Bonding of the NeuE input–output pads to the FFC was carried out by a previously reported conductive ink printing method[27]. In brief, a carbon nanotube solution (stock no. P093099-11, Tubes@Rice) was loaded into a pulled glass capillary printer head with an inner diameter of ~150 µm by capillary forces. The printer head was fixed to a holder (Warner Instruments) and then mounted onto a motorized micromanipulator (MP-285/M, Sutter Instrument), controlled by a rotary optical encoder (ROE-200, Sutter Instrument) and controller (MPC-200, Sutter Instrument). A custom-written LabVIEW program (available at http://meshelectronics.org/static/cnt-labview.zip) was used to set the starting and ending positions for each channel and drove the printer head to print the conductive ink in between automatically. Each channel of the NeuE could be individually connected to the corresponding channel on the FFC. The entire FFC with carbon nanotube-bonded NeuE was then cemented to the mouse skull by applying more Metabond quick adhesive luting cement on the top and side of the FFC and the exposed mouse skull while the other end of the FFC was uncovered and was connected to the recording system via a custom printed circuit board interface board. Recently, a simplified plug-and-play input–output connection methodology has been reported[50,51]. This strategy could be adapted to the NeuE design without affecting the crucial bioinspired implanted region of the NeuE design.

Postoperative care. After surgery, each mouse was returned to a cage equipped with a 37 °C heating pad. The activity of the mouse was monitored every hour until it was fully recovered from anaesthesia. Buprenex (Buprenorphine, Patterson Veterinary Supply) analgesia was given intraperitoneally at a dose of 0.05 mg per kg body weight every 12 h for up to 72 h post-surgery.

3D mapping of the NeuE–brain interfaces. *Histology sample preparation.* Mice with implanted NeuE were anaesthetized with ketamine/dexdomitor and transcardially perfused with ice-cold 40 ml 1 × PBS and 40 ml 4% formaldehyde (Electron Microscopy Sciences) at specified times post-injection, followed by decapitation. The scalp skin was removed and the exposed skull was ground for 10–20 min at 10,000 r.p.m. using a high-speed rotary tool (Dremel). Brains with the NeuE undisturbed were removed from the cranium and placed in 4% formaldehyde for 24 h and then transferred to 1 × PBS for another 24 h to remove any remaining formaldehyde. Brains were then embedded in 3% agarose (SeaPlaque agarose, Lonza) hydrogel, cut into blocks of 2 cm (length) × 2 cm (width) × 1 cm (height). Another NeuE probe was injected into the agarose hydrogel block to serve as a reference for the measurement of distance in subsequent micro-computed tomography (micro-CT) and vibratome sectioning steps (Supplementary Fig. 3). The hydrogel block containing the mouse brain was imaged by a micro-CT X-ray scanning system (HMX ST 225, Nikon Metrology) controlled by Inspect-X software (Nikon Metrology). CT Pro 3D software (Nikon Metrology) was used to calibrate the centres of rotation and to reconstruct the images. VGStudio MAX 3.0 software (Volume Graphics) was used to render and analyse the 3D reconstructed images. Distances between the reference NeuE and target NeuE as well as the angle θ (usually less than 5°) between the longitudinal axis of the target NeuE and the reference surface were measured from reconstructed images (Supplementary Fig. 3). The reference surface of the hydrogel block was then cut using a homemade sectioning stage according to measured angle θ to make this surface parallel to the longitudinal axis of the target NeuE. Finally, a mouse brain was sectioned into 500–1,000 µm slices using a vibratome (VT1000S vibrating blade microtome, Leica). The reference NeuE was used as a landmark to indicate the distance to the target NeuE to facilitate accurate sectioning. Because fluorescence from the target NeuE can be visualized with the aid of a wide-field epifluorescence microscope (Olympus) when it is 50–100 µm from the tissue surface, it is possible to adjust the sectioning such that one tissue slice includes the entire NeuE probe.

Tissue clearing and immunostaining. Transgenic mouse samples with endogenous expression of fluorescent proteins were used directly for refractive index matching and microscopy imaging as described in the next two sections. However, mouse brain slices that were targeted for immunostaining were first cleared using procedures adapted from the tissue clearing techniques CLARITY[30] and PACT[31]. After vibratome sectioning, brain slices were placed in 1 × PBS containing 4% (wt/vol) acrylamide (Sigma-Aldrich) and 0.25% (wt/vol) VA-044 thermal polymerization initiator (Fisher Scientific) at 4 °C for 3 days. The solution was replaced with fresh solution immediately before placing the brain slices in X-CLARITY polymerization system (Logos Biosystems) for 3 h at 37 °C. After polymerization, any remaining gel from the tissue surface was removed and the slices were rinsed with PBST (1 × PBS with 0.2% Triton X-100, Thermo Fisher Scientific) before placing them in electrophoretic tissue clearing solution (Logos Biosystems) at 37 °C for 3–5 days until the samples were translucent. After clearing, the brain slices were rinsed once with PBST containing 0.3 M glycine (Sigma-Aldrich), placed in fresh PBST containing 0.3 M glycine and incubated at 4 °C overnight. The samples were then placed in fresh PBST and gently shaken for 5 h, with the PBST replaced by fresh solution every hour. The brain slices were incubated with 1:100–1:200 primary antibodies, rabbit anti-doublecortin (Abcam) and/or rat anti-GFAP (Thermo Fisher Scientific) and/or goat anti-Iba1 (Abcam) in PBST for 4 days at 4 °C. After incubation, slices were placed in fresh PBST at RT to let excess antibody diffuse out of the tissue. The PBST was replaced with fresh solution every 8 h over the course of 2 days. The samples were then incubated with 1:100–1:200 secondary antibodies, goat anti-rabbit Alexa Fluor 488 (Abcam) or goat anti-rabbit Alexa Fluor 647 (Abcam), or donkey anti-rabbit Alexa Fluor 488 (Abcam) and/or donkey anti-rat Alexa Fluor 647 (Abcam) and/or donkey anti-goat Alexa Fluor 594 (Abcam) in PBST for 4 days at 4 °C. Slices were placed in fresh PBST containing 1 µg ml^{-1} DAPI (Sigma-Aldrich) at RT to let excess antibody diffuse out of the tissue and simultaneously stain nuclear DNA. The PBST with DAPI was replaced with fresh solution every 8 h over the course of 2 days. Note that DAPI was initially dissolved in DI water then diluted with PBST to make a concentrated stock solution (25 µg ml^{-1}) that was stored at 4 °C for no longer than 1 month before making a fresh stock. If necessary to improve light penetration for microscopy imaging, slices could be further incubated in Tris (Sigma-Aldrich) with 2% SDS (Sigma-Aldrich) and 0.3 M glycine at pH 6.8 at RT for 3 days then re-stained with DAPI.

Refractive index matching. Brain slices were glued at their edge to the bottom of 50-mm-diameter Petri dishes by Devcon 5 minute epoxy (ITW Polymers Adhesives) and then incubated in the refractive index matching solution PROTOS[52] (diatrizoic acid, Sigma-Aldrich; *N*-methyl-D-glucamine, Sigma-Aldrich; OptiPrep, Accurate Chemical and Scientific) or 80% glycerol:20% PBS (glycerol, Sigma-Aldrich) 24 h before microscopy imaging.

Microscopy imaging. Fluorescence images were acquired on a Zeiss LSM 880 confocal/multiphoton microscope (Carl Zeiss Microscopy) with a ×20 objective (numerical aperture 1.0, free working distance 5.6 mm). Near-infrared lasers were used for two-photon excitation of endogenously expressed fluorescent proteins in the transgenic mouse brain slices. Specifically, an 840 nm laser was used to excite RhBen, a 950 nm laser to excite YFP and a 920 nm laser to excite GFP. The bandpass filter for RhBen was 575–610 nm and that for YFP and GFP was 500–550 nm. Confocal images of cleared and immunostained brain slices were acquired using 405, 488, 561 and/or 633 nm lasers as the excitation sources for DAPI, Alexa Fluor 488, RhBen/Alexa Fluor 594 and/or Alexa Fluor 647, respectively. The corresponding bandpass filters were 411–496, 500–553, 562–624, 624–660 and/or 677–755 nm, respectively. Images were acquired by taking a tile scan together with Z stacks, with a voxel size of 0.2–0.6 µm (x) × 0.2–0.6 µm (y) × 0.4–2.5 µm (z) and tile scan overlap of 10%. YFP, GFP (GFAP), Iba-1, DCX, DAPI and NeuE are represented as green, cyan, magenta, yellow, blue and red in the composite images.

Chronic electrophysiological recording from awake and restrained mice. The following procedures were performed according to previous works[17] and are reproduced here for completeness. The electrophysiology of mice with implanted NeuE was recorded every day for ~30 min during the first half week post-implantation, every other day until the second week, followed by twice a week thereafter. Mice were restrained in a Tailveiner restrainer (Braintree Scientific) while their head-mounted FFCs were connected to an Intan RHD 2132 amplifier evaluation system (Intan Technologies) through a homemade printed circuit board. 0–80 set screws were used as references. Electrophysiological recordings were acquired with a 20 kHz sampling rate and a 60 Hz notch filter, while the electrical impedance of each recording electrode at 1 kHz was also measured by the same system and showed consistent values of <1 MΩ that allow for single unit recording measurements (Supplementary Fig. 14a). Thy1-YFP-16 mice were usually recorded for 3 months until they were transcardially perfused and underwent the same histology sample preparation procedure as described in the above section '3D mapping of the NeuE–brain interfaces'.

Reporting summary. Further information on experimental design is available in the Nature Research Reporting Summary linked to this article.

Code availability

The code used for data analysis is available from the corresponding author upon reasonable request.

Data availability

The data that support the findings of this study are available from the corresponding author upon reasonable request.

References

49. Rozenberg, B. Kinetics, thermodynamics and mechanism of reactions of epoxy oligomers with amines. *Adv. Polym. Sci.* **75**, 113–165 (1986).
50. Schuhmann, T. G., Yao, J., Hong, G., Fu, T.-M. & Lieber, C. M. Syringe-injectable electronics with a plug-and-play input/output interface. *Nano Lett.* **17**, 5836–5842 (2017).
51. Schuhmann, T. G. et al. Syringe-injectable mesh electronics for stable chronic rodent electrophysiology. *J. Vis. Exp.* **137**, e58003 (2018).
52. Murray, E. et al. Simple, scalable proteomic imaging for high-dimensional profiling of intact systems. *Cell* **163**, 1500–1514 (2015).

nature research

Corresponding author(s): Charles M. Lieber

Last updated by author(s): Jan 14, 2019

Reporting Summary

Nature Research wishes to improve the reproducibility of the work that we publish. This form provides structure for consistency and transparency in reporting. For further information on Nature Research policies, see Authors & Referees and the Editorial Policy Checklist.

Statistics

For all statistical analyses, confirm that the following items are present in the figure legend, table legend, main text, or Methods section.

n/a	Confirmed	
☐	☒	The exact sample size (*n*) for each experimental group/condition, given as a discrete number and unit of measurement
☐	☒	A statement on whether measurements were taken from distinct samples or whether the same sample was measured repeatedly
☐	☒	The statistical test(s) used AND whether they are one- or two-sided *Only common tests should be described solely by name; describe more complex techniques in the Methods section.*
☒	☐	A description of all covariates tested
☐	☒	A description of any assumptions or corrections, such as tests of normality and adjustment for multiple comparisons
☐	☒	A full description of the statistical parameters including central tendency (e.g. means) or other basic estimates (e.g. regression coefficient) AND variation (e.g. standard deviation) or associated estimates of uncertainty (e.g. confidence intervals)
☐	☒	For null hypothesis testing, the test statistic (e.g. *F*, *t*, *r*) with confidence intervals, effect sizes, degrees of freedom and *P* value noted *Give P values as exact values whenever suitable.*
☒	☐	For Bayesian analysis, information on the choice of priors and Markov chain Monte Carlo settings
☒	☐	For hierarchical and complex designs, identification of the appropriate level for tests and full reporting of outcomes
☒	☐	Estimates of effect sizes (e.g. Cohen's *d*, Pearson's *r*), indicating how they were calculated

Our web collection on statistics for biologists contains articles on many of the points above.

Software and code

Policy information about availability of computer code

Data collection	ZEN 2.1 software was used to acquire fluorescence images. Intan RHD2000 system was used to acquire electrophysiology data. Inspect-X software was used to acquire micro-CT X-ray data and CT Pro 3D software was used to reconstruct the images. No custom software or code was used for data collection.
Data analysis	Imaris 9, ImageJ, WaveClus 2.0 and custom MATLAB code were used for histology and electrophysiology data analysis. VGStudio MAX 3.0 software was used to render and analyze the micro-CT 3D reconstructed images.

For manuscripts utilizing custom algorithms or software that are central to the research but not yet described in published literature, software must be made available to editors/reviewers. We strongly encourage code deposition in a community repository (e.g. GitHub). See the Nature Research guidelines for submitting code & software for further information.

Data

Policy information about availability of data

All manuscripts must include a data availability statement. This statement should provide the following information, where applicable:

- Accession codes, unique identifiers, or web links for publicly available datasets
- A list of figures that have associated raw data
- A description of any restrictions on data availability

The data that support the findings of this study are included in the paper and the Supplementary Information. Further details are available from the corresponding author upon reasonable request.

Field-specific reporting

Please select the one below that is the best fit for your research. If you are not sure, read the appropriate sections before making your selection.

☒ Life sciences ☐ Behavioural & social sciences ☐ Ecological, evolutionary & environmental sciences

For a reference copy of the document with all sections, see nature.com/documents/nr-reporting-summary-flat.pdf

Life sciences study design

All studies must disclose on these points even when the disclosure is negative.

Sample size	Sample sizes were selected to achieve at least 80% power at a significance level of 0.05. The sample size for each experiment is detailed in the Supplementary Table 2.
Data exclusions	Exclusion criteria were pre-established: animals with failed surgeries or substantial acute implantation damage (>50 µL of initial liquid injection volume) were discarded from further experiments.
Replication	Replicate experiments on independent animals were performed to ensure the results are reproducible. Number of replicates for each experiment is detailed in the Replication section of Supplementary Information and Supplementary Table 2. Attempts at replication were successful and the conclusions were drawn from the analysis of multiple experiments.
Randomization	Mice were randomized into different experimental groups.
Blinding	Blinding was used during fluorescence image acquisition.

Reporting for specific materials, systems and methods

We require information from authors about some types of materials, experimental systems and methods used in many studies. Here, indicate whether each material, system or method listed is relevant to your study. If you are not sure if a list item applies to your research, read the appropriate section before selecting a response.

Materials & experimental systems

n/a	Involved in the study
☐	☒ Antibodies
☒	☐ Eukaryotic cell lines
☒	☐ Palaeontology
☐	☒ Animals and other organisms
☒	☐ Human research participants
☒	☐ Clinical data

Methods

n/a	Involved in the study
☒	☐ ChIP-seq
☒	☐ Flow cytometry
☒	☐ MRI-based neuroimaging

Antibodies

Antibodies used	Primary antibodies: Rabbit anti-doublecortin (Abcam, Catalog # ab18723, Lot # gr3224908-1); Rat anti-GFAP (Thermo Fisher Scientific Inc., Catalog # 13-0300, Lot # SF255147); Goat anti-Iba1 (Abcam, Catalog # ab5076, Lot # gr3195324-1). Secondary antibodies: Goat anti-rabbit Alexa Fluor 488 (Abcam, Catalog # ab150077, Lot # gr3203000-1); Goat anti-rabbit Alexa Fluor 647 (Abcam, Catalog # ab150079, Lot # gr3176223-3); Donkey anti-rabbit Alexa Fluor 488 (Abcam, Catalog # ab150073, Lot # gr3191541-1); Donkey anti-rat Alexa Fluor 647 (Abcam, , Catalog # ab150155, Lot # gr3188307-2); Donkey anti-goat Alexa Fluor 594 (Abcam, Catalog # ab150132, Lot # gr308670-2). All antibodies were diluted 1:100-1:200.
Validation	All the primary antibodies used in this study have been validated for immunohistochemistry on mouse brain tissues by the supplier and the customers including relevant citations as shown on the supplier's website. Our data also validate their use on cleared mouse brain tissues.

Animals and other organisms

Policy information about studies involving animals; ARRIVE guidelines recommended for reporting animal research

Laboratory animals	6~8-week male B6.Cg-Tg(Thy1-YFP)HJrs/J (Thy1-YFP-H, stock number 003782, Jackson Laboratory), B6.Cg-Tg(Thy1-YFP)16Jrs/J

Laboratory animals	(Thy1-YFP-16, stock number 003709, Jackson Laboratory), FVB/N-Tg(GFAPGFP)14Mes/J (GFAP-GFP, stock number 003257, Jackson Laboratory) and C57BL/6J mice (stock number 000664, Jackson Laboratory) were used in this study.
Wild animals	The study did not involve wild animals.
Field-collected samples	The study did not involve samples collected from the field.
Ethics oversight	All procedures were approved by the Animal Care and Use Committee of Harvard University. The animal care and use programs at Harvard University meet the requirements of the Federal Law (89-544 and 91-579) and NIH regulations and are also accredited by the American Association for Accreditation of Laboratory Animal Care (AAALAC).

Note that full information on the approval of the study protocol must also be provided in the manuscript.